In situ observation and kinetic modeling of the fundamental mechanisms underlying hydrogen sorption in forged Mg–Mg2Ni composites

Jing Wen, Patricia de Rango, Nathalie Allain, Marc Novelli, Thierry Grosdidier, Laetitia Laversenne

In situ observation and kinetic modeling of the fundamental mechanisms underlying hydrogen sorption in forged Mg-Mg_2Ni composites

Jing Wen[a,b,c,d*], Patricia de Rango[a], Nathalie Allain[b,d], Marc Novelli[b,d],

Thierry Grosdidier[b,d], Laetitia Laversenne[a*]

[a] Université Grenoble Alpes, CNRS, Institut Néel, 38000 Grenoble, France

[b] Univ Lorraine, Lab Etude Microstruct & Mecan Mat LEM3, CNRS UMR 7239, F-57045 Metz, France

[c] School of Material Science and Engineering, Dalian Jiaotong University, Dalian 116028, China.

[d] Univ Lorraine, Lab Excellence Design Alloy Met Low Mass Struct, F-57045 Metz, France

Corresponding authors:

Dr. Laetitia Laversenne: laetitia.laversenne@neel.cnrs.fr

Dr. Jing Wen: jing.wen@univ-lorraine.fr

Abstract. While Mg-Mg_2Ni composites are promising for hydrogen storage, their implementation is hindered by our incomplete understanding of absorption/desorption kinetics. Here, we combine *in situ* neutron diffraction with kinetic and microstructural analyses to uncover the sorption mechanism of deuterated hydrogen D_2 in a Mg-Mg_2Ni composite processed by fast forging. Phase transitions upon first absorption are found to be different from subsequent absorptions. The first absorption involves rapid formation of $Mg_2NiD_{0.3-x}$ followed by simultaneous formation of MgD_2 and Mg_2NiD_4. Kinetic modeling indicates that surface nucleation of the magnesium hydride is rate-limiting. Subsequent absorptions involve two phases, Mg and $Mg_2NiD_{0.3-x}$, which promote absorption. Kinetic modeling and microstructure analysis indicate that (1) MgD_2 nucleation occurs at the Mg-$Mg_2NiD_{0.3-x}$ interface and (2) Mg_2NiD_4 formation is kinetically controlled by deuterium diffusion through the growing Mg_2NiD_4 plate. In all desorptions, deuterium release starts by rapid decomposition of Mg_2NiD_4 into $Mg_2NiD_{0.3-x}$, followed by slower MgD_2 decomposition.

Keywords: Hydrogen storage; Mg-Mg_2Ni composites; Phase transformation; Deuterium sorption kinetics; *In situ* neutron diffraction; Microstructure

1. Introduction

The quest for hydride materials is crucial to place hydrogen vector at the core of the energy transition. Within this context, magnesium and its alloys keep receiving a great deal of attention for hydrogen storage owing to their light weight, high hydrogen storage capacity, low cost and abundance in Earth's crust (ranked as the 8th most abundant element). Moreover, Mg-based hydrides are considered as promising solid-state hydrogen storage media thanks to their large energy density and safety advantages over gas and liquid storage materials. However, the high thermodynamic stability of Mg-H bond as well as the sluggish sorption kinetics limit their technological applications [1-9]. To circumvent such hindering factors, many efforts have been devoted to modify the sorption properties of Mg-based materials, including catalyst doping and/or microstructure engineering using various processes such as high energy ball milling [1-4], melt-spinning [5,6] and severe plastic deformation [7-9].

Among processes that potentially improve hydrogen sorption properties, high-energy ball milling (HEBM) of MgH_2 powders with the addition of transition metals is widely used [1-4]. The improved performance can be explained by a boosted hydrogen diffusion in the material, which stems from the combination of reduced grain size, considerable amounts of structural defects, and large reactive surface area. However, sample activation (i.e. first hydridation of Mg), which is essential to produce the precursor MgH_2, remains very slow and requires high temperature (> 350 ℃) and pressure (up to 3 MPa) [1]. As a result, when large-scale production is desired, both the high pressure required for sample activation and HEBM process are prohibitive as they are time and energy consuming and require substantial manpower. Moreover, handling such pyrophoric powders raises safety concerns.

The combination of catalyst addition and structure engineering has proven to be an efficient way to promote hydrogen uptake and release kinetics in Mg-based hydrides [2-10]. In previous works [11,12], we have investigated how forging – the ancestral metalwork technique – leads to Mg-Ni composites with promising properties for hydrogen storage while offering a safe and efficient route to large scale manufacturing. We demonstrated that the Mg-Ni composites processed by fast forging exhibit markedly improved hydrogen sorption properties compared to the unprocessed powder. Of particular importance for practical applications, the hydrogen absorption and desorption kinetics were found to be accelerated with respect to conventional Mg-based samples. In spite of these results, the mechanisms leading to such improved behavior towards hydrogen storage have not been elucidated to date. In particular, the basal fiber texture of Mg, the presence of structural defects, and occurrence of microcracks formed upon fast forging were identified but their intimate connection to the faster hydrogen uptake kinetics remains to be established and deciphered [11].

The effect of adding Mg_2Ni to Mg was first investigated by Reilly in 1968 [13]. Remarkable sorption kinetics was reported for ball-milled samples [14] and more generally it is acknowledged that microstructure plays an important role [15]. For instance, an enhanced hydrogen dissolution was reported in the presence of crystal defects [16] or at the inter-grain region of nanostructured samples [17]. The role of the intermediate phase $Mg_2NiH_{0.3-x}$ has been mentioned in several studies [14-17] but the phenomena through which such intermediate phase enhances the sorption kinetics remain to be identified. *In situ* transmission

electron microscopy (TEM) has been employed to investigate Mg sorption properties [18-21] but this method has intrinsic drawbacks such as inelastic interactions with the sample and prominent surface effects due to the limited sample size [22]. Consequently, the hydrogen release mechanism obtained for thin samples – nano powders or thin foils – is not necessarily analogous to what operates in bulk samples.

Here, using an *in situ* experimental approach combining neutron diffraction, volumetric (thermodynamic) measurements, and microstructure analysis, we unravel the mechanisms that lead to improved hydrogen storage properties. In more detail, deuterated molecular hydrogen D_2 to trace the absorption/desorption mechanisms of a Mg-Mg_2Ni composite synthesized by annealing and forging. The sample under study has a composition of Mg - 22%wt Ni. Note that deuterium D is used here in place of hydrogen H to prevent strong incoherent scattering of neutrons and reduce background noise. Yet, all chemical phenomena remain unchanged. In fact, the thermodynamic properties are slightly affected by the substitution of hydrogen by its heavier isotope [23], but this influence can be ignored in our kinetic study. By coupling deuterium sorption kinetics with phase evolution, we directly uncover the role of intermediate phase in deuterium uptake and release in Mg-Mg_2Ni system. In addition, the combined kinetics modeling and microstructure observation for the partially deuterated sample allows us to understand the mechanisms involved in deuterium absorption/desorption at the microstructural scale. By deciphering the fundamental mechanisms leading to facilitated hydrogen sorption kinetics, this work paves the way for potential practical applications of forged Mg-based samples as efficient hydrogen storage media.

2. Experimental

Pellets of composition Mg-22 wt.% Ni were prepared under Ar atmosphere by manual grinding of Mg powder (99.8% purity, SFM, Switzerland) and Ni powder (99.5% purity, from Neyco, France) and cold compacted using a 1 T/cm^2 press. Subsequently, three pellets inserted into a thin cylindrical stainless sheath were heated by means of a retractable high frequency coil to 530° C and maintained for 30 min under Ar atmosphere. Finally, a 150 kg hammer was dropped from a height of 1.5 m at a rate of 4.7 m/s onto a piston. The piston was in direct contact with the sample which is positioned on the anvil of a specially designed chamber [11]. Prior to annealing and forging, the chamber was evacuated and rinsed with Ar

several times. After forging, the sample (2.10 g) was crushed into a coarse powder and poured into the 8 mm diameter molybdenum sample holder. The Mo airtight sample holder was equipped with a valve and a stainless-steel capillary tube that was connected to a volumetric rig allowing sorption measurements in the course of the neutron diffraction experiment. The sample temperature was monitored by the use of an external thermocouple placed above the sample holder (the whole system is inserted into a vanadium furnace). Note that throughout this manuscript activation will be used to refer to the first hydridation of the as-forged composites. However, we acknowledge that alloy activation, which consists of rendering the sample reactive to hydrogen, often correspond to different processes and conditions in the literature.

Neutron powder diffraction was performed at the CRG-D1b diffractometer at the Institute Laue Langevin (ILL) neutron source in Grenoble, France with a wavelength $\lambda = 2.52$ Å. The neutron wavelength was calibrated using a reference material consisting of $Na_2Ca_3Al_2F_{14}$ having a space group *I213* and a lattice parameter $a = 10.257$ Å. *In situ* diffraction patterns were recorded during the activation step under dynamic vacuum (heating up to a set point of 285°C and then maintaining the sample at this temperature for 55 min) and during three successive deuterium absorption/desorption sequences lasting 200 min. Due to this limitation in the time that can be probed using neutron experiments, the cycle for all absorptions was interrupted before full hydridation could be reached. As a result, the achieved storage is lower than the theoretical maximum deuterium capacity of the sample (11.14 wt%). We note that, upon data acquisition, some neutron diffraction patterns were unfortunately not recorded properly at the beginning of the first deuterium desorption. As a result, the data corresponding to the first 8 min of the first desorption is not availalble. The absence of data for the first 8 minutes makes it impossible to discuss the early stages of deuterium desorption. However, we stress that the missing data do not affect our analysis using kinetic modeling since the coupled pressure/volume data were determined independently. Moreover, while no mitigation strategy could be used to palliate this drawback, we believe that our analysis remains robust and accurate as the second desorption data are complete.

Diffraction patterns were collected every 1 min and analyzed according to the Rietveld method using the FullProf Suite [24]. Absorption and desorption steps were performed by submitting the sample to 20 bars and 1.5 bars of deuterium D_2, respectively. On the one hand,

the lower pressure of 1.5 bar was selected as it is below the equilibrium pressure of Mg/MgH_2 at the working temperature of 285°C. On the other hand, the higher pressure of 20 bar was chosen as it lies above the equilibrium pressure of Mg/MgH_2 and Mg_2Ni/Mg_2NiH_4. Gaseous deuterium was set in contact with the chamber containing the sample using a buffer tank at a controlled pressure. Along the experiment, the pressure was monitored using a digital pressure transducer while the temperature within the oven was maintained constant using a regulation thermocouple. It is worth noting that the low thermal conductivity of the Mg-Mg_2Ni system, its high reaction enthalpy (ΔH = -75 kJ/mol H_2) together with the large amount of the powders used during the experiment (2.10 g) can lead to non-negligible temperature variations inside the reactor during deuterium loading and unloading. However, if occurring, such temperature increases upon exothermal absorption would tend to slow down the reaction so that the fast kinetics observed in the present work should be considered as a lower boundary (similarly, upon desorption, the temperature decrease for this endothermal reaction would also be slowed down).

Microstructure observations before and after deuterium sorption were performed using a combined analysis of X-ray diffraction (XRD) and field emission scanning electron microscopy (SEM) coupled with electron backscatter diffraction (EBSD). XRD macro-texture measurements were carried out to have a better representation of the crystallographic texture of the fast forged samples. In total, five pole figures $(0002)_{Mg}$, $(10\bar{1}0)_{Mg}$, $(10\bar{1}1)_{Mg}$, $(10\bar{1}2)_{Mg}$ and $(11\bar{2}0)_{Mg}$ have been measured and the texture components were recalculated using the ATEX software [25]. For microstructure observation, the sectioned faces from the bulk sample were mechanically polished using SiC papers with grits from 1000 to 4000 followed by electrolytic polishing in an electrolyte of 62% phosphoric acid and 38% ethanol (at 2V and 15°C for 3 min). To collect the high-quality Kikuchi patterns, the samples were Ar ion polished with a PECS-II GATAN using 3.0 keV beam energy under dual beam condition (with a gun angle of 2° and for about 2h). EBSD characterization was then performed using a JEOL-6500F SEM equipped with the AZtec acquisition software package at a step size of 0.10 μm. The Euler angles (φ_1,ϕ,φ_2) provided by EBSD represent a set of three characteristic rotations from the sample coordinate system to the crystal coordinate system. With the Euler angles, the coordinate transformation matrix can be established between the two coordinate systems. With the coordinate transformation matrices of the two crystals, we can express the normal directions of the twinning planes, habit planes and interface planes to the sample

coordinate system (X-Y-Z) and project these directions to the XOY plane by stereographic projection [26]. The coincident poles of the common directions and the common planes normal resolved using the rotational coordinate transformation matrices written in a MATLAB software allow us to determine the twinning planes, habit planes and interface planes between two crystals [27,28].

3. Results

3.1 Structure and microstructure changes upon deuteration

3.1.1 Phases in presence upon absorption and desorption

Fig. 1 presents the Rietveld refinements of the neutron diffraction patterns taken at different times during the first deuterium absorption (initial sample activation). The two peaks positioned at 2θ = 70° and 105° correspond to the molybdenum sample holder. Fig. 1a shows the refined pattern collected before deuterium absorption. The starting phases Mg, Ni and Mg_2Ni were detected but a low fraction of magnesium oxide (2.50 wt%) was noticed. Fig. 1b, 1c and 1d show the refined patterns recorded at 10, 30 and 60 min of deuterium uptake, respectively. At the beginning of deuterium absorption, a progressive shift of the diffraction peaks corresponding to the solid solution $Mg_2NiD_{0.3-x}$ is observed. This result indicates that a single Mg-Ni-D phase exists in the system as phase coexistence would necessarily lead to different sets of diffraction peaks. After 5 min of deuterium absorption, two deuteride phases – identified as MgD_2 and Mg_2NiD_4 – start to form almost simultaneously. The binary MgD_2 deuteride has a crystal structure of the type tetragonal body centered (*P42/mnm*). Its lattice parameters are a = 4.509 Å and c = 3.019 Å as determined using Rietveld refinement of the neutron diffraction patterns. The ternary deuteride, Mg_2NiD_4, has a face-centered cubic structure (*Fm-3m*) with lattice parameter of a = 6.512 Å. As can be seen from Fig. 1, the peak intensities of the deuteride phases MgD_2 and Mg_2NiD_4 increase with time upon absorption. The weight fractions of each phase as a function of time are shown in Fig. 2a, while Table 1 presents the weight fractions and lattice parameters extracted through Rietveld refinements. The formation kinetics of these phases as well as the deuterium uptake/release kinetics will be addressed in Section 3.2. Note that the weight fraction of MgO (2.50 ± 0.15 wt%) is not included in Table 1.

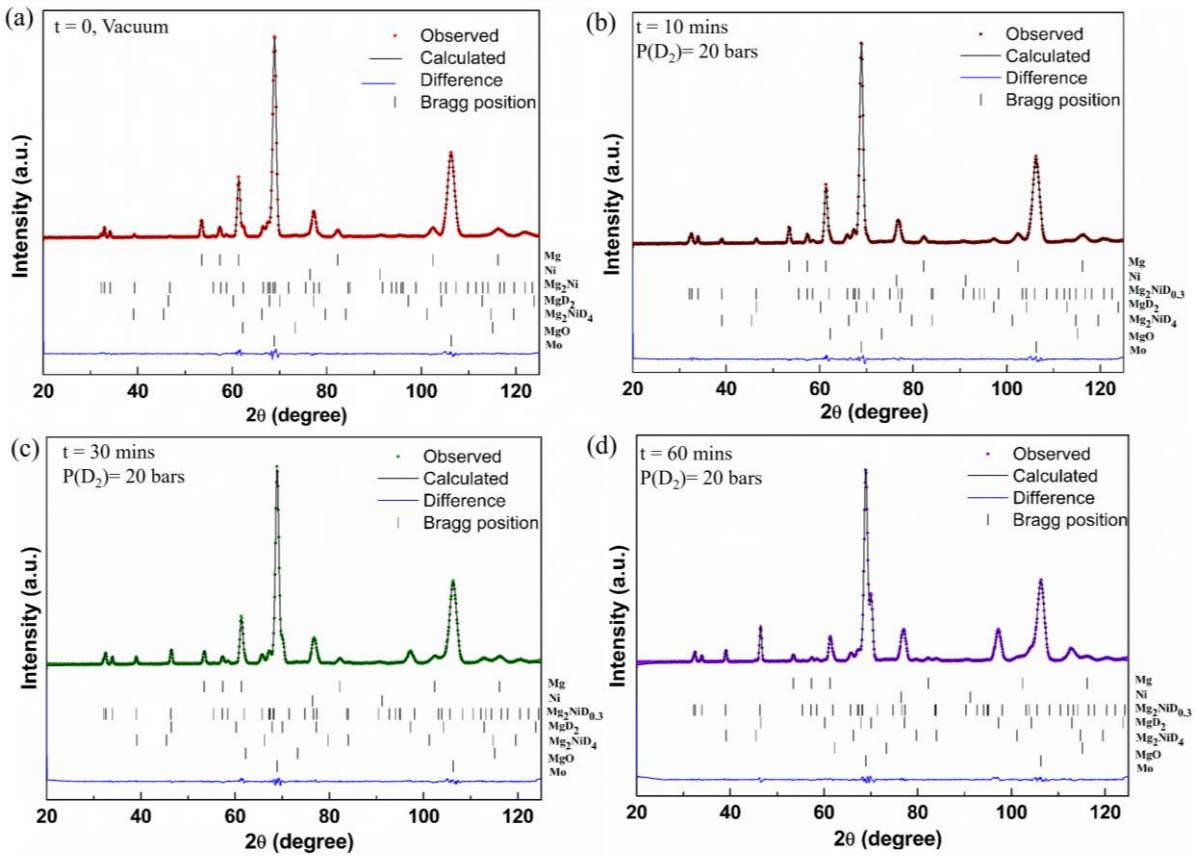

Fig. 1. Neutron diffraction patterns and the related Rietveld analyses at 285°C at different times upon first deuteration: (a) corresponds to data taken under vacuum at t = 0 while (b), (c) and (d) correspond to data under a deuterium pressure of 20 bars at t = 10 min, 30 min and 60 min, respectively.

Table 1 Weight fraction of each phase calculated at different times during the first deuterium absorption.

Uptake time (min)	Weight fraction (wt. %)				
	Mg (P 63/m m c, a = 3.2297 ± 0. 0001 Å, c = 5.2444± 0. 0003 Å)	Mg_2Ni (P 62 2 2, a = 5.2269 ± 0. 0002 Å c = 13.3092 ± 0. 0007 Å)	$Mg_2NiD_{0.3-x}$ (P 62 2 2, a = 5.2533± 0. 0002 Å c = 13.4764± 0. 0008 Å)	MgD_2 (P 42/m n m, a = 4.5091± 0. 0002 Å c = 3.0193± 0. 0004 Å)	Mg_2NiD_4 (F m -3 m, a = 6.5128 ± 0. 0001 Å)
0	57.56 ± 1.05	40.84 ± 2.08	—	—	—
10	52.64 ± 1.33	—	40.48 ± 2.60	3.14 ± 0.11	0.26 ± 0.11
30	44.15 ± 0.90	—	39.51 ± 2.02	12.20 ± 0.25	1.34 ± 0.12

60	25.59 ± 0.63	–	30.03 ± 2.16	36.45 ± 0.80	5.24 ± 0.18
200	11.87± 0.67	–	16.13 ± 0.42	50.93 ± 0.47	17.36 ± 0.23

Note that the total composition does not amount to 100% as a small amount of MgO was also observed (*see text*). The lattice parameters indicated in the first row were estimated at an uptake time of 10 min for $Mg_2NiD_{0.3-x}$, MgD_2 and Mg_2NiD_4. In contrast, the lattice parameters for Mg and Mg_2Ni were taken at the initial time of the hydridation.

.

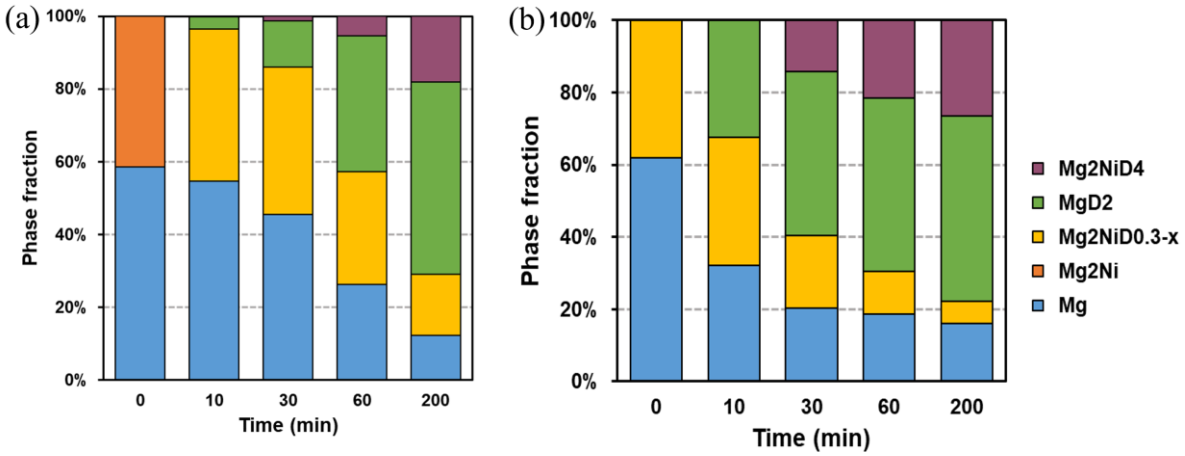

Fig. 2. Weight fractions of each phase as a function of time as extracted through Rietveld refinements of the diffraction patterns collected under a deuterium pressure of 20 bars upon (a) the first deuterium absorption (activation) and (b) upon the second absorption.

Fig. 3 shows the change in unit cell volume corresponding to the solid solution $Mg_2NiD_{0.3-x}$ during deuterium sorption. Upon the first absorption, the solubility of deuterium in $Mg_2NiD_{0.3-x}$ lattice can be identified from the increase in the unit cell volume. After 45 min of deuterium absorption, the lattice parameters of $Mg_2NiD_{0.3-x}$ become constant, therefore indicating that the dissolution of deuterium atoms within the lattice reaches saturation. The increase of the unit cell volume reaches 7.5 $Å^3$ – a value in agreement with literature data for the solid solution of stoichiometry $Mg_2NiD_{0.3}$ [29,30]. The saturation of the solid solution is even confirmed by the formation of the hydride Mg_2NiD_4, which is visible after 30 minutes in Fig. 2 (the weight fraction of the $Mg_2NiD_{0.3-x}$ phase decreases as the Mg_2NiD_4 starts to form). Upon desorption, deuterium release is only partial as a deuterium pressure of 1.5 bar is maintained in contact with the sample. Under such applied pressure and temperature conditions, desorption of the $Mg_2NiD_{0.3-x}$ phase is not complete [16, 30, 31]. The transformation between the $Mg_2NiD_{0.3-x}$ and Mg_2NiD_4 phases upon sorption results in an

noticeable change in the lattice volume of the $Mg_2NiD_{0.3-x}$ solid solution. Upon subsequent absorption/desorption, the lattice volume of the $Mg_2NiD_{0.3-x}$ solid solution increases/decreases quickly in the first minutes. Then, the content of deuterium (D%) in the solid solution varies in accordance to the pressure/temperature conditions.

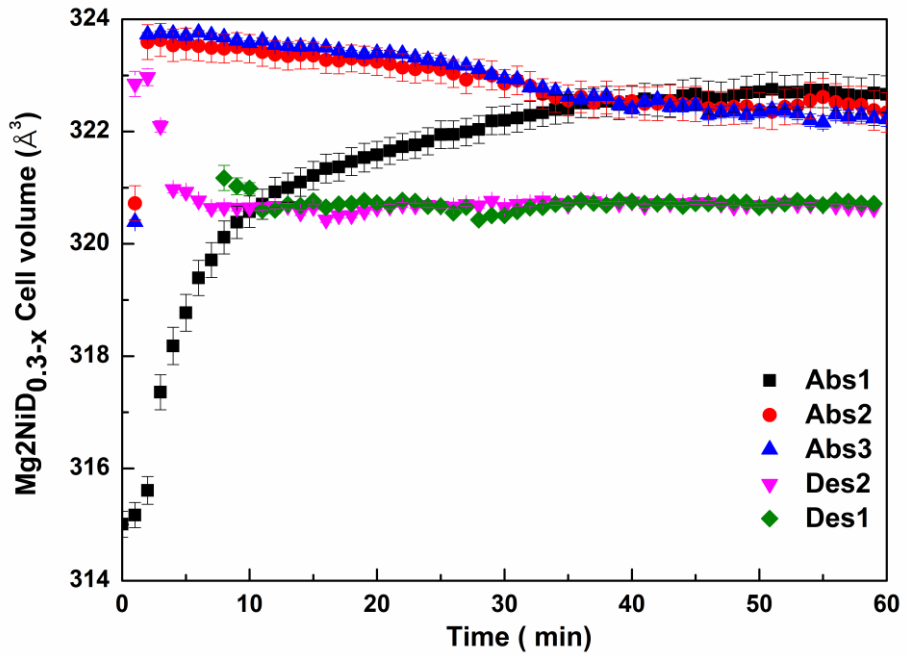

Fig. 3. Evolution of the unit cell volume of the $Mg_2NiD_{0.3-x}$ solid solution recorded during successive deuterium absorptions and desorptions as labelled in the figure. Note that due to operational issues upon data acquisition during the first 8 min, some neutron diffraction patterns are missing for the beginning of the first deuterium desorption.

3.1.2 Microstructure

Before deuteration (Figs. 4a-4c), the initial microstructure consists of fragmented Mg_2Ni lamellae embedded in a textured Mg-matrix (See Ref. [11] for more details). According to the Mg-Ni phase diagram, the composition of Mg-22wt%Ni is hypoeutectic with primary Mg_2Ni and Mg-Mg_2Ni eutectic. In line with this prediction, it is interesting to note that Figs. 4a and 4d display blocks of primary Mg_2Ni. Fig. A1(a) in the Supplementary Material shows the XRD pattern obtained for the as-forged Mg-Mg_2Ni composite. The high intensity of the Mg (0002) diffraction peak implies the presence of basal-fiber texture in the forged sample as confirmed by the inserted pole figure recalculated from the XRD measurement. This fiber texture is characterized by a majority of *c*-axes approximately aligned with the forging direction (FD). The formation of this {0001} basal fiber texture is related to the slip systems $\{0001\}< 11\bar{2}0 >$ operating on the basal planes of the magnesium structure [32,33]. In the

phase map superimposed with band contrast (Fig. 4b), the Mg and Mg_2Ni phases are colored in red and blue, respectively while the black pixels correspond to the non-indexed areas due to porosities and cracks. The presence of these porosities and cracks (marked by red arrows in Fig. 4a) was proposed as preferential diffusion paths for deuterium atoms. Fig. 4c, which shows the Inverse Pole Figure (IPF) map of Mg phase for the as-forged Mg-Mg_2Ni composite, indicates that the Mg grains exhibit a certain degree of preferential orientation along the FD.

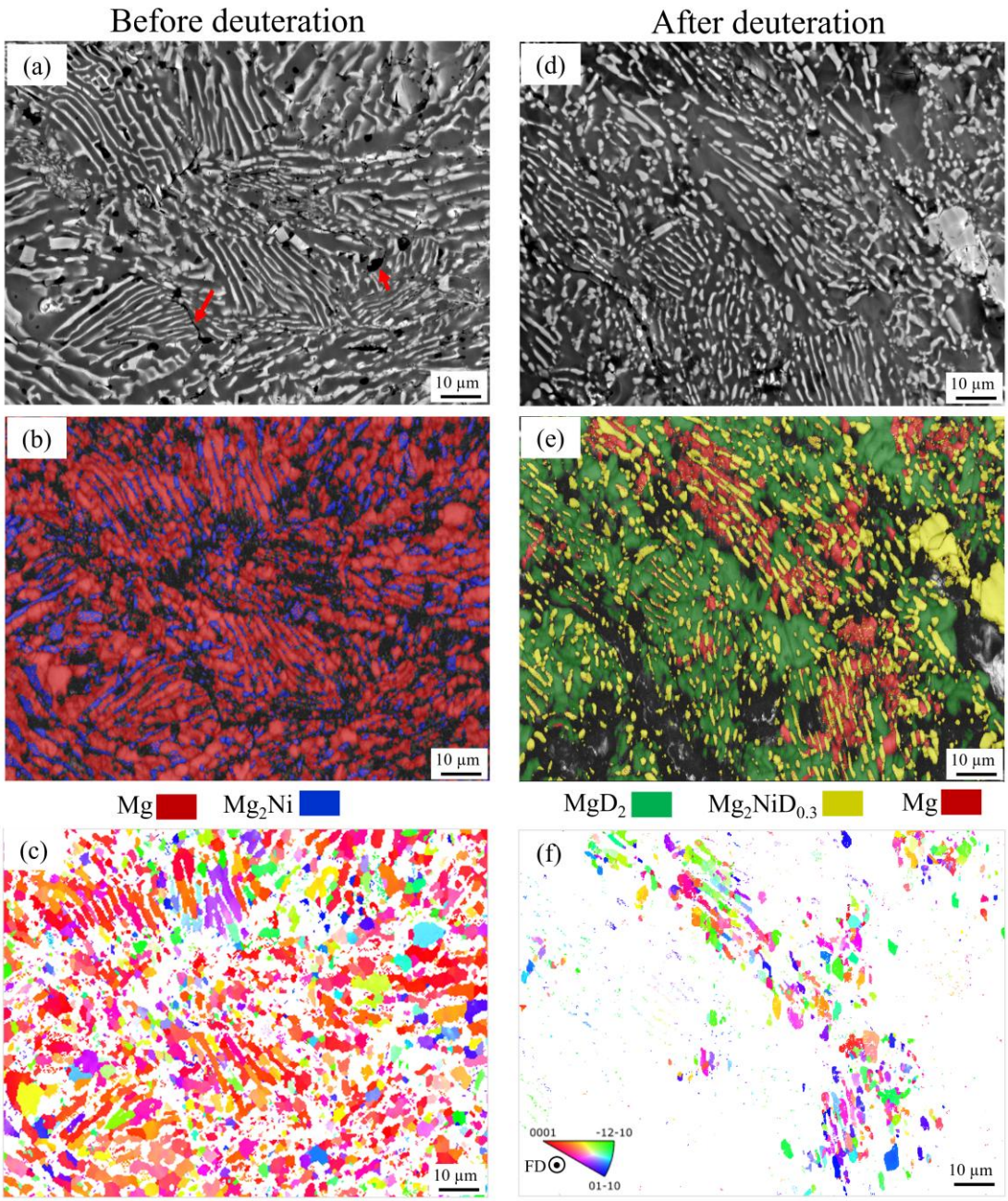

Fig.4. Microstructure before and after deuteration on a cross-section of the sample. (a), (b) SEM-SEI images; (d), (e) phase maps superimposed with band contrast; and (c), (f) IPF maps of Mg phase (note that the microstructure after deuteration is taken from the sample that is partially deuterated).

Fig. 4d shows the microstructure observed after three deuterations of the sample. As explained above, the sample is partially deuterated and contains 8.512 wt.% of deuterium (the theoretical maximum deuterium uptake for this sample is 11.14 wt.%). A tendency towards rounding is observed for the initial lamellae constituents. Deuterium absorption can be considered as an annealing process under deuterium gas atmosphere. This process happens during annealing to minimize the surface area/energy. Additionally, we noticed that the initial lamellae structure becomes severely/heavily fragmented as the volume changes upon phase transformation induce internal stresses. The phase map superimposed with band contrast for the partially deuterated sample is shown in Fig. 4e, where the MgD_2, $Mg_2NiD_{0.3-x}$, and Mg phases are indicated by green, yellow and red colors, respectively. Almost no Mg_2NiD_4 phase was detected by EBSD scanning, which is due to the fact that the beam decomposes Mg_2NiD_4 upon ion polishing as shown in Fig. A.1(b) in the Supplementary Material (which shows the XRD patterns before and after ion polishing). In fact, most of the Mg_2NiD_4 is transformed into $Mg_2NiD_{0.3-x}$ upon ion polishing. The decomposition of Mg_2NiD_4 into $Mg_2NiD_{0.3}$ during ion polishing is driven by a combination of localized heating, which leads to deuterium desorption and physical sputtering (where deuterium atoms are preferentially removed from the sample surface). Both effects result from the interaction of the ion beam with the sample, which reduces the deuterium concentration and transforms Mg_2NiD_4 into $Mg_2NiD_{0.3}$. In this context, other preparation techniques than ion polishing could have been used. Yet, the alterations induced by technique do not drastically affect our main conclusions based on SEM-EBSD analysis. Indeed, the expected alterations are essentially located at the surface without significantly modifying the microstructure including the grain morphology, grain orientations and phase distributions.

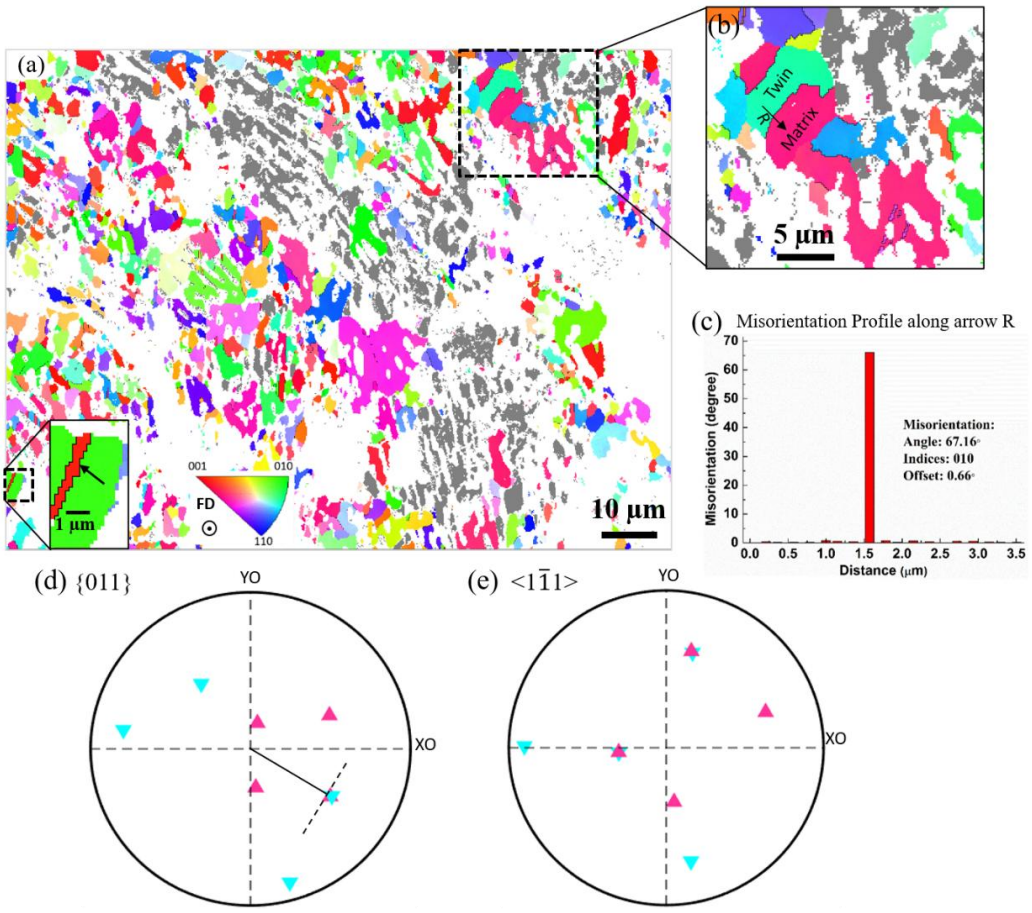

Fig. 5. Determination of twinning in MgD_2 after three deuterations of the composite. (a) IPF map of MgD_2 superimposed with twin boundaries and the Mg-phase map (the untransformed Mg phase is in grey); (b) Zoom in a micrometer-sized twin corresponding to the selected area; (c) Misorientation profile along the arrow R in (b); (d, e) Stereographic projections of twinning plane {011} and twinning direction <1$\bar{1}$1>, respectively. We note that opposite grain boundaries are the twin boundaries.

For the partially deuterated sample, the remaining undeuterated Mg phase exhibits random grain orientation with respect to FD as shown in the IPF map of Mg in Fig. 4f. Another interesting aspect observed for the partially deuterated sample is the presence of twins within the MgD_2 grains. This can be seen in the IPF map superimposed with twin boundaries and the phase map of Mg in Fig. 5a (where the untransformed Mg phase is in grey). The size of the twins (marked by the black arrows) varies from tens of nanometers to several micrometers. For instance, a micrometer sized twin with curved boundaries is shown in Fig. 5b. The orientation relationship between the initial MgD_2 matrix and the twinned region can be expressed by a rotation around the axis <100> with a misorientation angle of 67° as presented in Fig. 5c (where the misorientation profile corresponding to the arrow R is shown in Fig. 5b). Furthermore, using the method developed by F. Zimmermann and M. Humbert [26,27] to determine the twinning planes by means of the EBSD technique, the twinning system is found to be {011} <1$\bar{1}$1> (as obtained using the stereographic projections of twinning plane {011} in Fig.

5d and twinning direction <1$\bar{1}$1> in Fig. 5e, respectively). In the {011} pole figure, the dashed line outlines the surface plane trace of the twin plate. In addition, the solid line connects the center of the pole figure with the poles corresponding to the twinning plane and perpendicular to the surface plane traces of the twin plate. Numerous studies [19,34-37] have reported that twined microstructures can significantly improve the hydrogen uptake/release kinetics by acting as high diffusivity paths for hydrogen. The generation of twins related to deuterium uptake kinetics will be discussed in Section 4.1.

3.2 Deuterium absorption

3.2.1 Phase evolution and absorption kinetics

The 3D plots of neutron diffraction patterns were used to follow the time-dependent phase structural transformations upon deuterium absorption/desorption. Fig. 6a shows the phase evolution during the first 60 min of deuteration. Fig. A.3 in the Supplementary Material shows the same data as Fig. 6(a,b) but with a 2D representation displaying the shift of the Bragg peaks. The sequence of phase transformations during the first deuterium absorption (activation sequence) can be described as follows:

$$Mg_2Ni + \frac{0.3-x}{2} D_2 \rightarrow Mg_2NiD_{0.3-x} \quad (1)$$

$$Mg + D_2 \rightarrow MgD_2 \text{ and } Mg_2NiD_{0.3-x} + \frac{3.7+x}{2} D_2 \rightarrow Mg_2NiD_4 \quad (2)$$

The deuterium uptake is initiated by the formation of the $Mg_2NiD_{0.3-x}$ solid solution during the first 10 minutes (Fig. 2a). This stage is followed by the growth of two deuterides, MgD_2 and Mg_2NiD_4, that form almost simultaneously. The rate of the Mg → MgD_2 reaction is faster than that of the $Mg_2NiD_{0.3-x}$ → Mg_2NiD_4 reaction. After 200 min of deuterium absorption (Table 1), the weight fractions indicate that 79% of Mg is transformed into MgD_2 while only 53% of $Mg_2NiD_{0.3-x}$ is transformed into Mg_2NiD_4.

Upon the second deuterium absorption (Fig. 6b), the sequence of phase transformation is found to be very different from the first deuterium absorption. This second absorption is characterized by two successive steps:

$$Mg + D_2 \rightarrow MgD_2 \quad (1)$$

$$Mg_2NiD_{0.3-x} + \frac{3.7+x}{2} D_2 \rightarrow Mg_2NiD_4 \quad (2)$$

The transition of $Mg_2NiD_{0.3-x}$ into Mg_2NiD_4 only starts after 17 minutes. This characteristic time corresponds to the time at which about two thirds (62.5 wt.%) of the Mg phase has been already transformed into MgD_2.

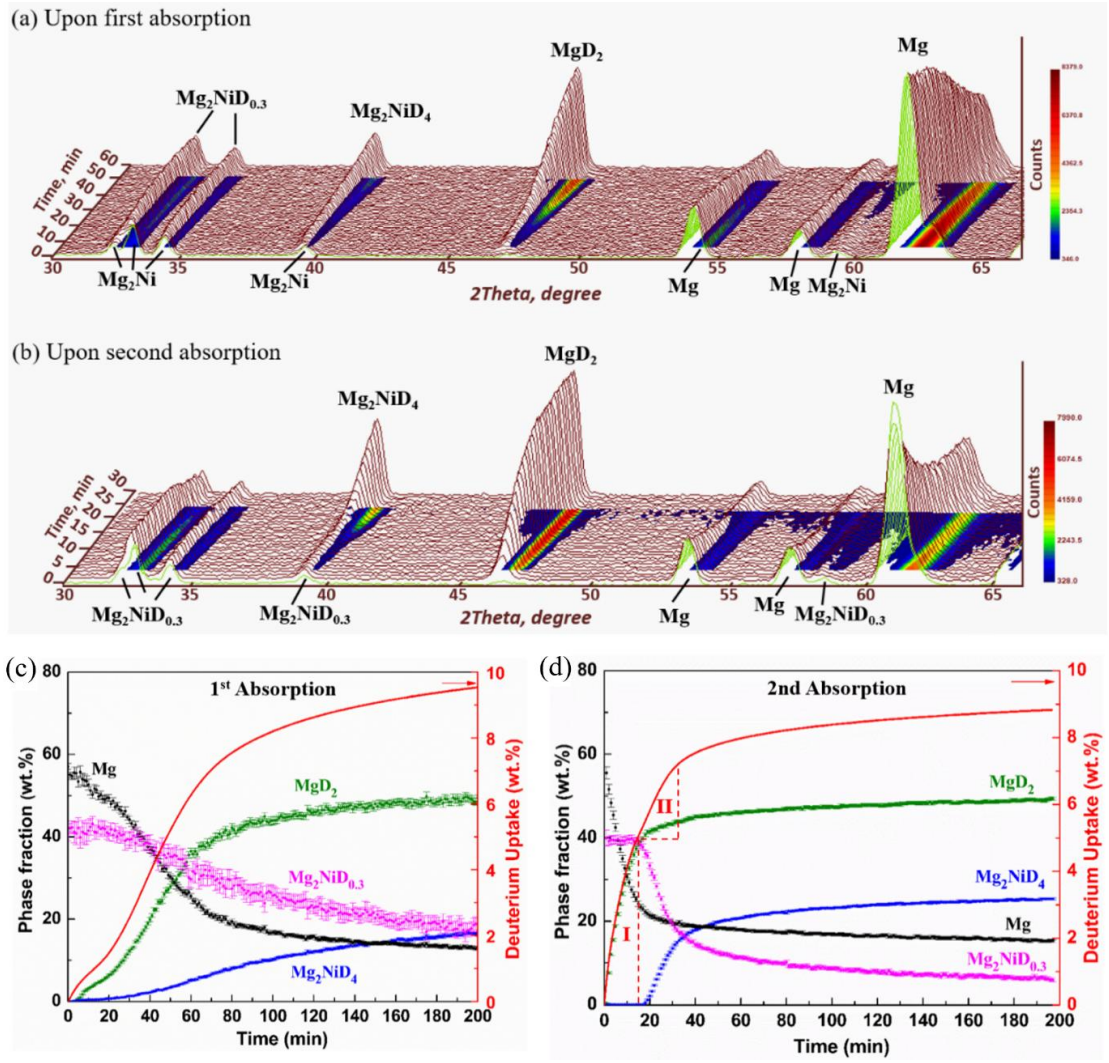

Fig. 6. 3D plots of neutron diffraction patterns. For the sake of visualization, only a part of the collected diffraction data (2θ region 30 - 65°) is shown. (a) First absorption (initial sample activation). (b) Second absorption. (c, d) Deuterium uptake kinetics coupled with phase evolution during first and second deuterium absorptions, respectively.

To reveal the role of phase constituent in deuterium absorption, the deuterium uptake kinetics and the change in phase content are superimposed on the same plot in Figs. 6c and 6d. The deuterium uptake observed during the first deuterium absorption shows a multi-stage process (Fig. 6c). The reaction rate slows down after a few minutes, increases up to 70 min, and then decreases again to reach a slower rate. The time dependent change in the MgD_2 weight fraction displays a trend similar to the deuterium uptake kinetics, which indicates that the first deuterium absorption is mainly dominated by the formation of the MgD_2 phase. For the composition Mg-22 wt.% Ni, a theoretical maximum deuterium uptake of 11.14 wt.% is

expected. In contrast, after the first deuteration, 8.39 wt.% of deuterium uptake was recorded – a value corresponding to 75.8% of the expected uptake. This apparent maximum uptake is due to a deliberate choice to stop the experiment after 200 minutes because of the time constraints imposed on large scale instruments such as neutron diffractometers.

Our experimental results show that faster deuterium uptake occurs in the subsequent absorptions compared to the first sorption cycle. For the second absorption (and the following absorptions which are not shown here for the sake of clarity), a two-stage deuterium uptake takes place and then the absorption kinetics becomes much slower after about 40 minutes (Fig. 6d). The first absorption stage is directly related to the formation of the MgD_2 phase as no formation of Mg_2NiD_4 is observed. After about 17 minutes, a second absorption stage dominated by the $Mg_2NiD_{0.3-x} \rightarrow Mg_2NiD_4$ transition takes place. In contrast, at that time, further formation the MgD_2 phase slows down significantly. Both formation kinetics (MgD_2 and Mg_2NiD_4) are faster than during the first absorption and the proportion of Mg_2NiD_4 phase is significantly higher at the end of the second cycle. However, the deuterium uptake recorded after 200 minutes of absorption is only slightly lower than the one recorded for the first absorption. This limited capacity on further cycling, which was already observed on volumetric measurements performed on forged Mg-Ni samples [11], remains unexplained to date. While both hydrides form simultaneously during the first uptake, the two-step mechanism observed *in situ* by neutron diffraction on further cycling seems to prevent reaching the maximum storage capacity (as the formation of MgD_2 is blocked when Mg_2NiD_4 appears).

3.2.2 Kinetics of deuterium sorption determined by use of solid-gas reaction models

The commonly applied formalisms used to determine key kinetic parameters (e.g. hydriding /dedydriding limiting steps) are (1) the Johnson-Mehl-Avrami (JMA) model [38-40], (2) the contracting volume (CV) model [41,42], and (3) the Jander model [43]. The mathematical descriptions of these models are given in Table 2, where the reacted/transformed fraction and the kinetic constant are represented by x and k. (1) The JMA model depicts deuterium absorption/desorption as three successive processes: nucleation, growth and impingement. Random nucleation occurs on the surface and/or in the bulk of the particles. The growth of random nuclei can be controlled by the motion of the metal/deuteride interface at a constant

velocity or by a diffusion-controlled growth mechanism with a decreasing interface velocity. We note that Avrami's equation can be considered with different values for *n* in the range 1-4 [44]. However, we choose in the present study to restrict our kinetic modeling investigation to *n* = 1, 2 and 3 only for a sake of simplification." (2) The CV model describes the growth of a new phase starting from the surface of the particle or at the grain boundary, with the growth proceeding towards the center of the particle. In other words, it assumes that a thin layer of nuclei already exists at the surface. However, if deuterium diffusion through the growing phase is rate-limiting, the metal/deuteride interface moves at a decreasing velocity and the corresponding contracting volume model is labelled as CV2/3. (3) Another diffusion-controlled model was proposed by Jander [43] which assumes that the metal/hydride interface area is constant for diffusion and the volume of the particle is not changed before and after hydridation/dehydridation. The Jander model can be seen as oversimplified because these two assumptions are not always justified in practice.

Table 2 Equation, description and label of the different applied kinetic models [38-43].

Model equation	Rate-limiting process	Label
$[-\ln(1-x)]^{1/n} = kt$ n : Avrami exponent	The growth of random nuclei at a constant interface velocity, with n = 1, 2 and 3 for one-dimensional growth (JMA1), two-dimensional growth (JMA2) and three-dimensional growth (JMA3)	JMA1 JMA2 JMA3
$1-(1-x)^{1/n} = kt$ n : dimensionality	The growth of contracting volume at a constant interface velocity, with one-dimensional (CV1), two-dimensional (CV2) and three-dimensional (CV3)	CV1 CV2 CV3
$[1-(1-x)^{1/3}]^2 = kt$	Diffusion of hydrogen through the hydride layer	Jander
$1-2x/3-(1-x)^{2/3} = kt$	3D diffusion-controlled mechanism with the metal/hydride interface moving at a decreasing velocity	CV2/3

3.2.2.1 Kinetics of deuterium absorption upon activation

To perform the kinetic analysis, the transformed fractions are derived from *in situ* neutron diffraction patterns (Rietveld refinements) as well as from volumetric measurements. It should be mentioned that the transformed fraction derived from volumetric measurements is

only suitable for single-phase formation. The inferred transformed fractions are then substituted in the equations provided in Table 2. The equations are formulated in such a way that a linear behavior with time should be observed if the assumed underlying process controls the reaction. Table A.1 in the Supplementary Material presents the fitting results corresponding to MgD_2 and Mg_2NiD_4 formation rates calculated from Rietveld refinements analysis during the first deuteration process. The best fits are obtained for R^2 (fitting goodness) and Y_o (y axis intercept) close to 1 and 0, respectively.

The very first minutes of the activation sequence corresponds to the deuterium enrichment of the $Mg_2NiD_{0.3-x}$ solid solution as shown by the volume expansion of the Mg_2Ni lattice (Fig. 3). The time scale of the process is not suitable for kinetic analysis as it is too fast to be analyzed accurately. After this very fast first step, deuteration proceeds in two dominant sequences. The one that occurs during the first hour mainly concerns the deuterium absorption in Mg. The kinetic model that best describes deuterium absorption in Mg from the start of the reaction is model JMA2. The kinetic constant *k*, which is obtained by fitting the experimental values to the JMA2 model, describes the magnesium deuteration reaction well for the first 60 minutes after exposure of the sample to deuterium. However, after this time, a slowing down of the reaction occurs when 60% of the transformation is achieved. We could not find a satisfactory model to depict the formation of the remaining 12 wt% MgD_2 within the time interval of 60 to 200 minutes. A possible explanation for this observation is the limited deuterium diffusion into Mg due to impingement of MgD_2 particles and, consequently, the prevailing nature of the second transformation (formation of Mg_2NiD_4). Regarding the formation of the ternary hydride Mg_2NiD_4, none of the models considered in this work correctly represents the reaction progress during the first 50 minutes (prevailing MgD_2 growth). During this time, the rate of formation is very low, reaching 9% after 50 minutes. After 50 minutes, the model that best fits the reaction kinetics until the end of the experiment is the one in which the rate is limited by a diffusion process (CV2/3 or Jander). The diffusive nature of the process in this regime is confirmed by comparing the experimental and calculated reaction rates for Mg_2NiD_4 (Fig A.2 in the Supplementary Material). Our results are in good agreement with reports on very slow hydrogen diffusion through the Mg_2NiD_4 phase [45,46].

From the results above, we conclude that, upon activation, deuterium absorption occurs in a very fast initial step consisting of hydrogen enrichment of the $Mg_2NiD_{0.3-x}$ solid solution. This

step is followed by deuteration of magnesium according to a nucleation and growth process starting from the $Mg/Mg_2NiD_{0.3-x}$ interphase boundaries. Due to MgD_2 impingement, the deuteration of Mg is drastically slowed down and $Mg_2NiD_{0.3-x}$ transforms into Mg_2NiD_4 by a limited diffusion mechanism. This last interpretation is fully consistent with previous work [47] on the hydride nucleation rate in Mg samples; hydrides can nucleate quickly at the Mg surface or $Mg_2NiD_{0.3-x}$/Mg interfaces, therefore leading to the observed CV2/3 model. Such surface nucleation leads to the formation of a hydride shell that behaves as a diffusion barrier for subsequent hydrogen absorption. As a result, this phenomenon makes the core of the samples difficult to transform into a hydride phase and hence reduces the hydrogen capacity.

3.2.2.2 Kinetics of deuterium absorption of activated composites

In order to understand the origin of the two-stage behavior observed for cycled samples, we focus in the following on the kinetic mechanisms involved in the second deuterium absorption. Table A.2 in the Supplementary Material presents the fitting results corresponding to MgD_2 and Mg_2NiD_4 formation rates calculated from Rietveld refinements during the second deuteration process. During the second deuterium absorption process, the fits point to a diffusion-controlled mechanism (CV2/3) being responsible for the $Mg \rightarrow MgD_2$ transition from t = 0 to 17 min. Since only the MgD_2 phase forms during the first step of the deuterium absorption, the formation rate of MgD_2 can also be derived from the deuterium uptake divided by the theoretical maximum capacity reached when only MgD_2 forms. While the volumetric data were recorded every 4s, each neutron diffraction pattern was recorded every 1 min. Thus, considering that a better time resolution is expected from volumetric measurements of deuterium uptake, they were used to confirm the kinetic mechanism leading to MgD_2 formation. The corresponding analysis confirms that the CV2/3 model correctly accounts for the second deuterium absorption from t = 0 to 17 min (with R^2 = 0.99825 and $t_0 \sim 0$). The factor $k = 0.5639 \times 10^{-4}$ s^{-1} is slightly lower than that calculated from Rietveld analyses but of the same order of magnitude.

To further analyze the MgD_2 rate-limiting mechanism, the measured reaction rate was compared with the ones derived from the k factor obtained by fitting each model (Fig. 7). As expected, an excellent match is observed between the CV2/3 model and the experimental volumetric data recorded between t = 0 to 17 min (Fig. 7a). A rather good agreement is also

observed with the Jander model which is very close to the CV2/3, while the other models do not fit at all the experimental data. Similarly, the same behavior is also observed for the third cycle (not shown here), which further confirms that the MgD_2 formation after the first activation is controlled by a diffusion mechanism with the migration of the Mg/MgD_2 interface at a decreasing velocity. However, after t = 17 min, a very large discrepancy is observed between the MgD_2 reaction rate calculated from the diffusion model and the one deduced from the Rietveld refinements (Fig. 7b). As evidenced by *in situ* neutron diffraction measurements, the transition of $Mg_2NiD_{0.3-x}$ to Mg_2NiD_4 only starts after 17 min of reaction and the formation of MgD_2 abruptly slows down as soon as Mg_2NiD_4 starts to form.

In a similar approach, the Mg_2NiD_4 reaction rate derived from Rietveld refinement analysis was carried out by fitting the data against each model. A good agreement was only reached from t = 17 to 33 min (Table A.2 in the Supplementary Material). Fig. 7c and Fig. 7d show the comparison of the experimental Mg_2NiD_4 reaction rate with those derived from the k factors for each kinetic model. The deuterium absorption kinetics seems to be controlled by a one-dimensional nucleation and growth (JMA1) of Mg_2NiD_4 plates. In this model, a rather fast nucleation is followed by the motion of the $Mg_2NiD_{0.3-x}/Mg_2NiD_4$ interface at a constant velocity. A slowdown of the $Mg_2NiD_{0.3-x} \rightarrow Mg_2NiD_4$ reaction is observed after about 33 min, when about 50% of the solid solution is transformed into Mg_2NiD_4 (Fig. 7d). This is most likely due to the impingement of the Mg_2NiD_4 grains, which may hinder further diffusion of deuterium atoms to the $Mg_2NiD_{0.3-x}/Mg_2NiD_4$ interface.

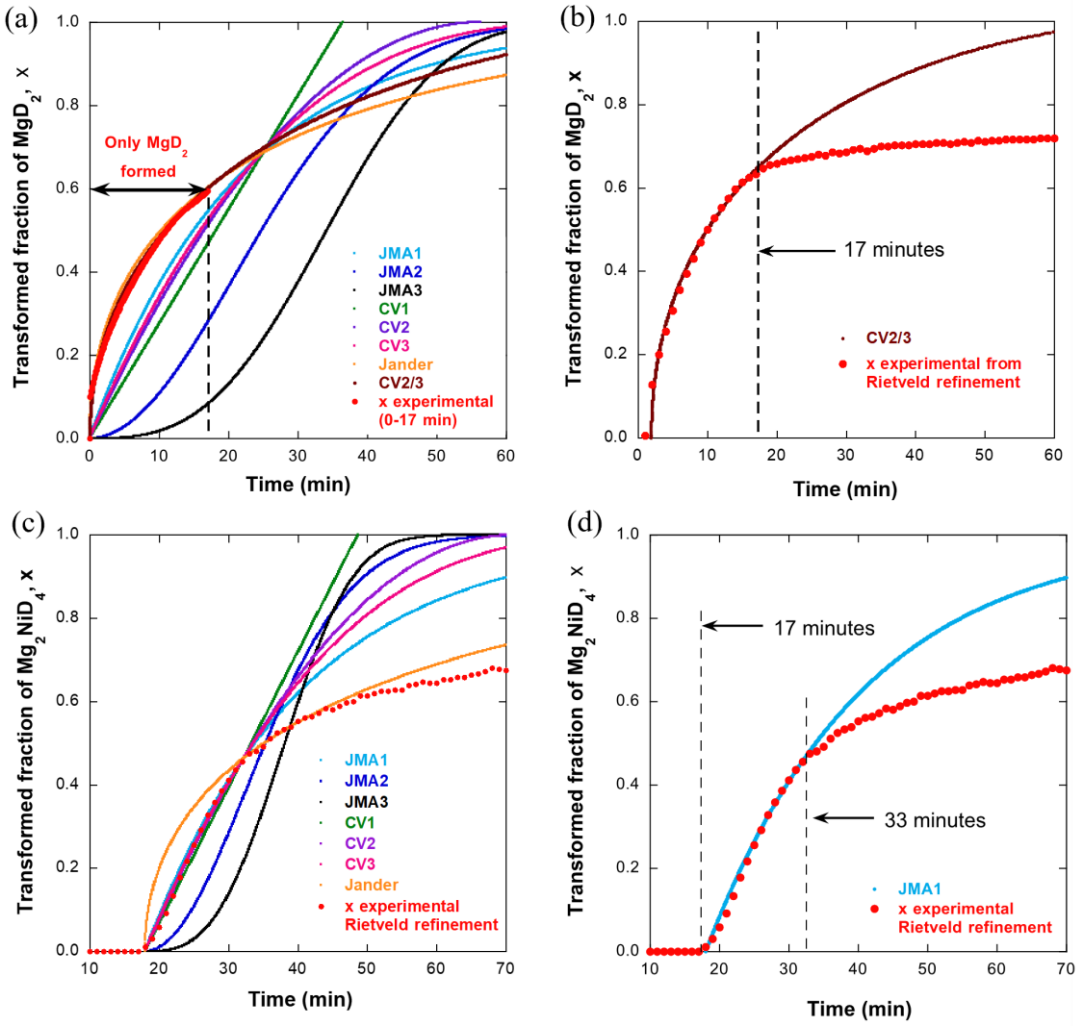

Fig. 7. Comparison between the experimental hydride reaction rates (in red) and the reaction rates calculated from the *k* factors obtained for each kinetic model (other colors according to the legends provided in the graphs). These data and predictions were obtained for deuterium absorption in the second cycle. (a) MgD_2 reaction rate deduced from volumetric measurements. (b) MgD_2 reaction rate deduced from Rietveld refinement of neutron diffraction patterns. (c,d) Mg_2NiD_4 reaction rate deduced from Rietveld refinement of neutron diffraction patterns.

3.3 Deuterium desorption

The time-dependent phase structural transformations observed during the first and second deuterium desorption processes are depicted in Figs. 8a and 8b, respectively. The deuterium release kinetics with respect to phase transformation are described in Figs. 8c and 8d. The release of deuterium is similar for both the first and subsequent desorptions. Since the sample was not fully deuterated, it already contains Mg and $Mg_2NiD_{0.3-x}$ phases at the beginning of the desorption stage. The deuterium desorption of the MgD_2-Mg_2NiD_4 system proceeds in reverse order of the deuterating process as observed from the second absorption. First, the

Mg_2NiD_4 transforms into the solid solution $Mg_2NiD_{0.3-x}$ and deuterium; this process is completed in a very short period of time (< 8 min). Subsequently, the MgD_2 transforms into Mg and deuterium; this second step is a rather slow process lasting for 40 min. As the desorption from Mg_2NiD_4 occurs rather fast, analysis of the kinetics parameters of the decomposition process $Mg_2NiD_4 \rightarrow Mg_2NiD_{0.3-x}$ is not possible in the context of the present study. The fitting of the Mg reaction rate from 6 to 60 minutes ($0.23 < x < 0.99$) corresponds to the entire $MgD_2 \rightarrow$ Mg reaction. The CV2 model fits with a very good $R^2 = 0.9993$ until the reaction ends (99%). Such analysis suggests that the reaction involves a constant velocity of the reaction front. This is confirmed by the comparison of the experimental rate with the rates calculated from the *k* factors obtained for each model (Fig. 9).

According to our *in situ* observations, the well-known 'hydrogen pump' effect associated with Mg_2NiH_4 [5-9] is directly linked to the rapid formation of $Mg_2NiH_{0.3}$ into Mg_2NiH_4. This is in line with the *in situ* investigation of the hydrogen release mechanism in bulk Mg_2NiH_4 using ultra-high voltage TEM combined with Synchrotron X-ray diffraction (SXRD) [16]. According to this work, the temperature for the removal of hydrogen atoms from the solid solution $Mg_2NiH_{0.3}$ must be higher than 500°C under vacuum. Indeed, the desorption temperature is directly dependent on the pressure, the higher the pressure the higher the temperature. Following this previous example, it can be assumed that the complete desorption temperature at 1.5 bar would be even higher than 500°C. This interpretation explains why there is still 36.5 wt% of $Mg_2NiD_{0.3-x}$ left in the sample at the end of the desorption under such *T*/*P* conditions.

The kinetic modeling reported in the present study provides insights into the reactive mechanisms at play. Yet, such studies should be considered with caution as this type of modeling only suggests possible mechanisms which helps identify limiting rates. In this context, while further work is needed to fully validate our proposed scenario, we note that it is the first time that hydrogen absorption/desorption kinetics of such bulk-sized Mg-Mg_2Ni composites is investigated at multi-scales, this will be deeply addressed in discussion part.

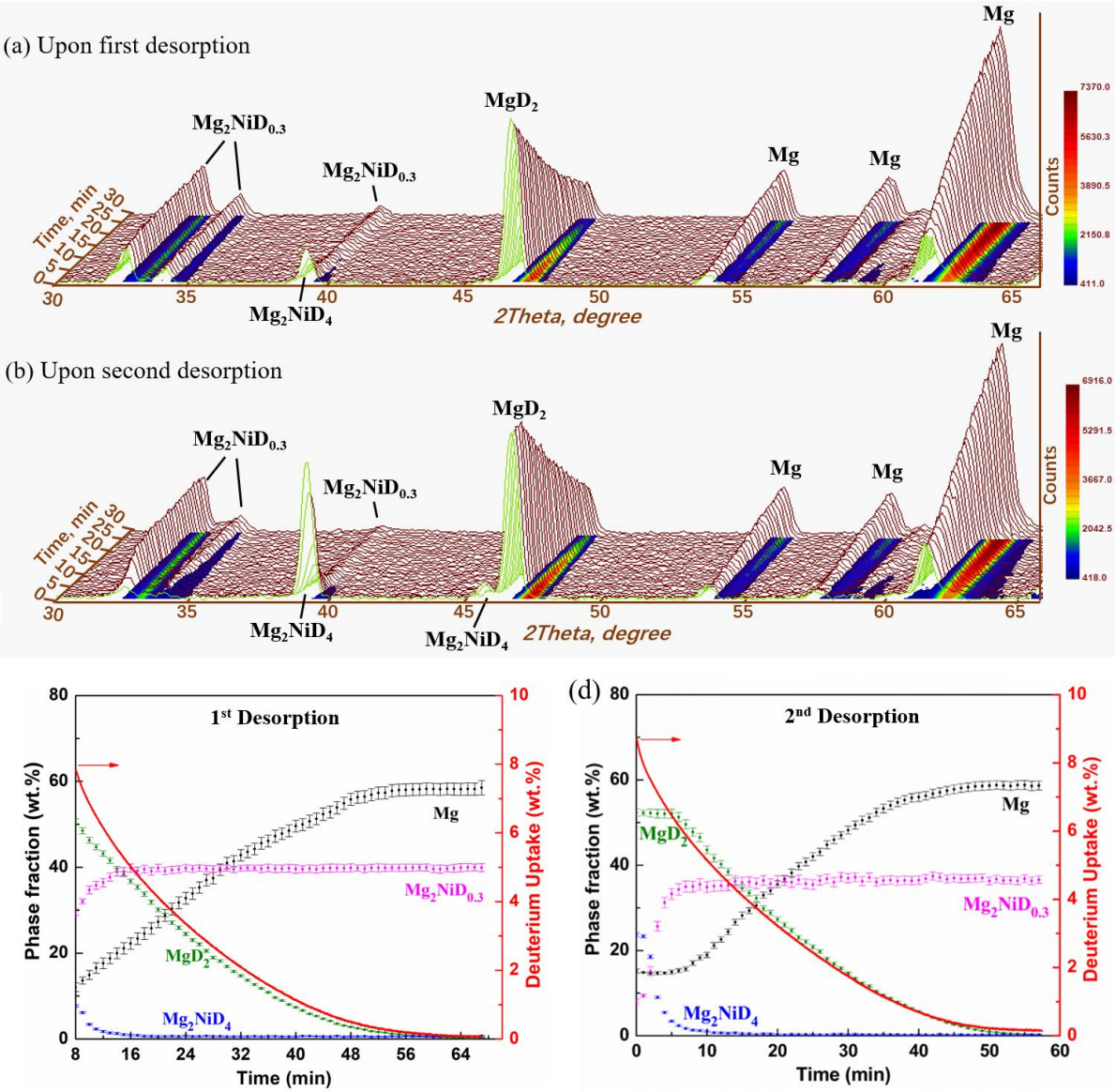

Fig. 8. 3D plots of neutron diffraction patterns upon (a) first desorption and (b) second desorption. For the sake of visualization, we show only a part of the collected diffraction data (2θ in the range 30–65°). (c,d) Deuterium release kinetics coupled with phase evolution: during the first and second deuterium desorptions, respectively. Note that due to operational issues upon data acquisition during the first 8 min, some neutron diffraction patterns are missing for the beginning of the first deuterium desorption. Nevertheless, the characteristics of phase evolution upon deuterium desorption can be still drawn from Fig. 8b as done in the main text. In contrast, due to the absence of data for $t < 8$ min for the first desorption, the comparison between the beginning of the desorption process for the first and second runs cannot be made.

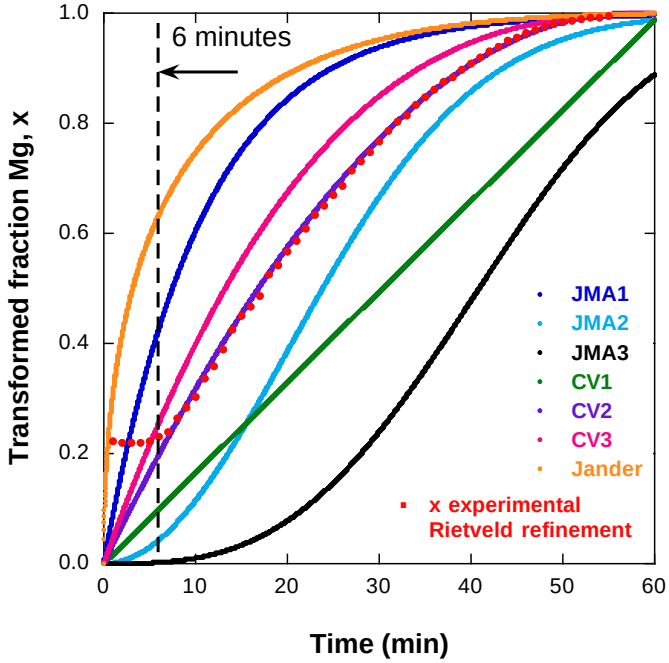

Fig. 9. Comparison between the experimental Mg formation rate (in red) at the interval 6 – 60 minutes and the reaction rates calculated from the *k* factor obtained for each model (other colors according to the legend provided in the graph). The data correspond to the second desorption.

4. Discussion

4.1 Multifactor mechanisms of the activation (first absorption) of Mg-Mg_2Ni composites

The hydrogen absorption rate is not only determined by the applied temperature and pressure, but also by several factors controlling the various activation barriers. The latter are related to hydrogen physisorption, chemisorption, penetration, diffusion and the nucleation/growth of the hydride [48]. Of particular relevance to the present work on forged samples, the microstructure also plays a key role. Hydrogen absorption in a crystalline solid can either occur as a result of isotropic diffusion and random nucleation or through preferential nucleation along certain favorable crystal axes. Due to the lower packing density of the atoms, hydrogen diffusion along grain/phase boundaries is usually faster than through the lattice. Moreover, grain/phase boundaries are favorable nucleation sites for the formation of hydride [7]. Mg-based alloy/powder materials are known to be strongly sensitive to the formation of magnesium oxides at the sample surface, which prevents H_2 dissociation and subsequent penetration, diffusion and hydride formation. Therefore, the kinetics of hydrogen/deuterium absorption during the very first absorption (initial sample activation) and the associated phase transformations strongly depend on the initial surface state of the material. Prior to deuterium absorption, a small amount of MgO (2.50 wt.%) was detected by neutron diffraction due to unavoidable surface oxidation of Mg. The oxide layer at the Mg surface, which cannot be

reduced by thermal effects at the experiment temperature (285°C), inhibits the surface nucleation of MgD_2. As compared with Mg, the Mg_2Ni phase is less reactive with oxygen owing to its lower chemical affinity with oxygen [49]. The rapid dissolution and diffusion of deuterium atoms in the Mg_2Ni lattice leads to the initial formation of the $Mg_2NiD_{0.3-x}$ solid solution (Fig. 2) – as evidenced by the significant increase in unit cell volume observed in the very first minutes (Fig. 3). The strong interconnection between the Mg_2Ni lamellae (Fig. 4) facilitates the deep diffusion of deuterium and contributes to a homogeneous and rapid reaction in all Mg_2Ni regions of the sample linked to the surface of the particles. The kinetic analysis performed above shows that MgD_2 formation is controlled by a 2D nucleation and growth process (JMA2) for the initial two-thirds of the reaction. This can be explained by the deuterium rapidly diffusing in the bulk of the particles through the solid solution and reaching the interphase boundaries of $Mg/Mg_2NiD_{0.3-x}$, where MgD_2 potentially begins to nucleate. The reaction rate decreases once two-thirds of MgD_2 is formed. Activation of the composite (first deuterium absorption) is accompanied by the appearance of cracks and twins as recapitulated below. Our present experimental results show an increased rate of deuterium absorption in magnesium in activated composite. It is worth noting that the diffusivity of hydrogen has been shown to be several orders of magnitude faster at grain boundaries than in the bulk of particles [48]. As shown in Section 3.2.2 where 3D diffusion modelling was used to describe the $Mg \rightarrow MgD_2$ transformation, the absorption mechanism at this stage of the reaction in the activated composite is the one classically observed in bulk Mg particles. The Mg/MgD_2 interface moves with decreasing velocity towards the interior of the particle and the diffusion of deuterium through the MgD_2 layer becomes the limiting factor.

In addition to kinetic modeling analysis, the underlying mechanisms involved in hydrogen/deuterium absorption can be further analyzed using a complementary analysis of the microstructure. In particular, we focus on the $Mg\text{-}MgD_2$ phases as they represent approximately two thirds of the volume of the sample with a homogeneous distribution. As shown in the present work, during deuteration, the hexagonal close-packed (*hcp*) lattice of magnesium expands by approximately 31.4%, which leads to a transformation of the *hcp* metal sublattice into the deformed body-centered cubic sublattice. Because of this deformation, this sublattice becomes tetragonal for MgD_2. If we assume that the phase transformation from *hcp*-Mg to *bct*-MgD_2 follows the orientation relationship (OR) $(100)_{MgH_2}//(0001)_{Mg}$ and $[001]_{MgH_2}//[\bar{1}\bar{1}20]_{Mg}$ proposed by Schober [51], the OR planes

mismatch and the OR directions mismatch are calculated to be about 53% and 6.5%, respectively. Twinning could provide a means to accommodate the mismatch between the parent Mg phase and the product MgD_2 phase during phase transformation [34, 51-53]. For the partially deuterated sample, twins were observed within the MgD_2 grains (Fig. 5). For the observed twinning system {011} <1$\bar{1}$1>, the twinning shear is calculated to be 0.4687. The temperature where the MgD_2 deuteride precipitates is well below those where the rate of self-diffusion of Mg is predominant. Therefore, the transition from Mg into MgD_2 should proceed by a shearing or shuffling process. Our work shows that twins are formed due to stress accommodation upon hydride growth as previously reported in the Mg-H [19, 51], Zr-H [52] and Ti-H [53] systems (for which hydride precipitation was studied in the framework of the martensitic transformation theory). By combining the analysis of the microstructure with that of the hydrogen sorption kinetics, it is believed that the observed twins account for hydrogen enhanced diffusivity [7,19,34-37]. We note that twins and dislocations and in general phase and grain boundaries as well as dislocations play a crucial role in hydrogen absorption and desorption. In this context, the observed twins correspond to coherent boundaries with only mirror symmetry which provide paths for hydrogen diffusion. As such, we think that they are sufficient to explain at least qualitatively the observed improved hydrogen sorption kinetics.

As for Mg_2NiD_4 during the first absorption step, its formation occurs when the accommodation of deuterium atoms within the $Mg_2NiD_{0.3-x}$ lattice reaches saturation (Fig. 2 and also Fig. 10a). This phenomenon occurs simultaneously with the appearance of MgD_2, therefore indicating that the deuterium pressure (20 bars) exceeds the equilibrium pressure of both Mg_2Ni-Mg_2NiD_4 and Mg-MgD_2 systems at the considered temperature (285°C). The thermodynamical conditions for the formation of both deuterides are met. After 50 minutes, both MgD_2 and Mg_2NiD_4 reaction rates are controlled by a diffusion mechanism as suggested by our kinetic modeling. Deuterium diffusion through Mg_2NiD_4 has been shown to be at least two orders of magnitude slower than through the $Mg_2NiD_{0.3-x}$ solid solution [46]. As a result, the presence of this phase and its increasing abundance significantly slows down the diffusion of deuterium towards magnesium. The presence of the ordered deuteride of the Mg_2Ni intermetallic hinders the diffusion of deuterium in the composite. It is therefore advisable to operate under controlled conditions of pressure and temperature in order to promote the formation of the $Mg_2NiD_{0.3-x}$ solid solution over the growth of the Mg_2NiD_4 hydride.

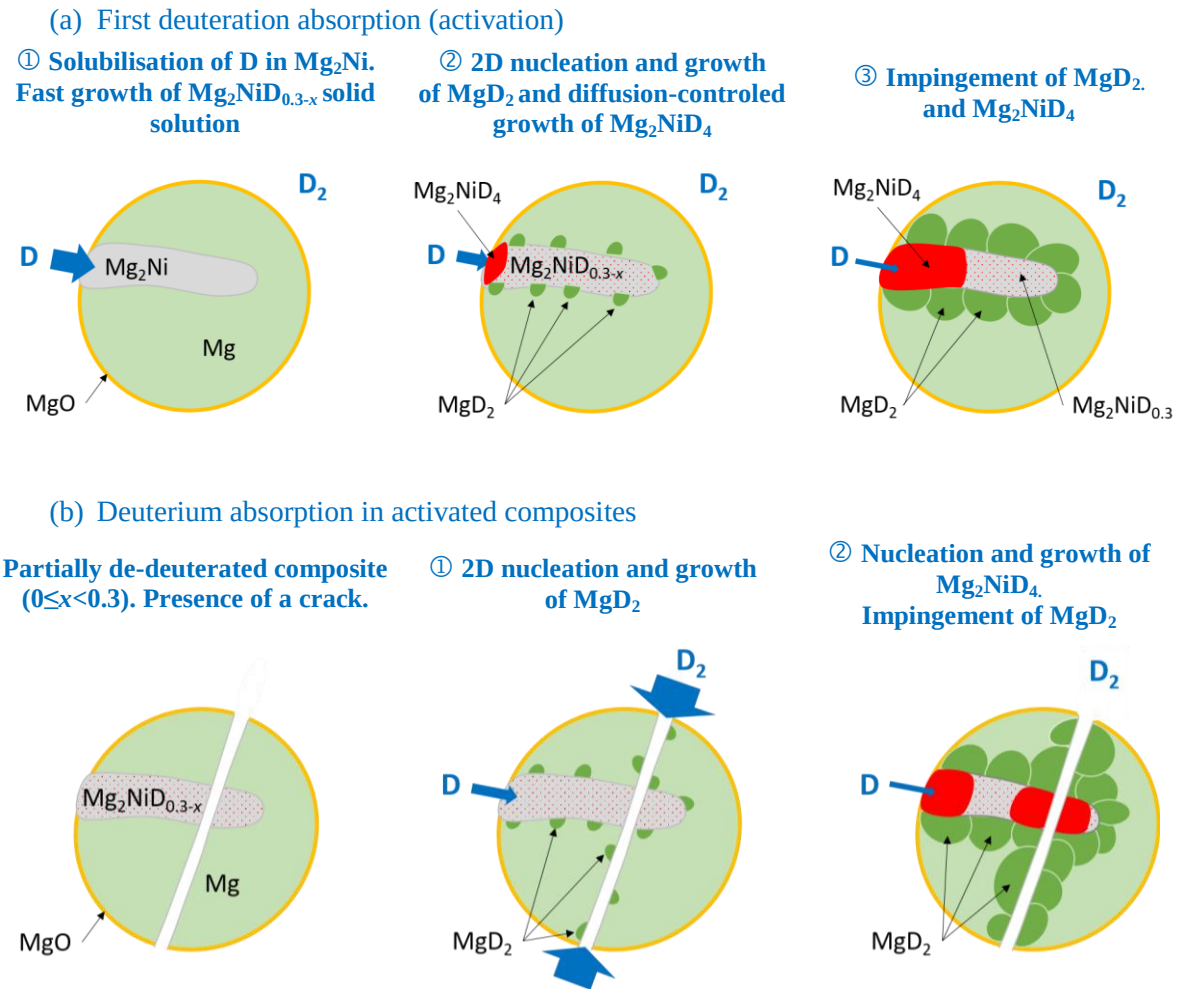

Fig. 10. Schematic illustration of the deuterium-induced microstructure evolutions upon (a) the first deuterium absorption (sample activation) and (b) the subsequent absorption (activated Mg-Mg_2Ni composite with a crack).

4.2 Sorption mechanisms in activated Mg-Mg_2Ni composites

As described in Section 4.1, the activation process is the result of a combination of favorable chemical and mechanical phenomena. Deuterium diffuses quickly through the sample via the $Mg_2NiD_{0.3-x}$ solid solution (bypassing the barriers formed by the oxidized Mg surfaces). Nucleation of MgD_2 occurs at the interphase boundaries between $Mg_2NiD_{0.3-x}$ and Mg, resulting in microstructural changes that increase the concentration of preferential paths for hydrogen diffusion (such as twins of size varying from tens of nanometers to several micrometers which have been highlighted by EBSD analysis). SEM observations show that the Mg_2NiD_4 lamellae are highly fragmented after the first deuteration. The large area EBSD

mapping provides the spatially resolved information about phase distribution, crystallographic grain orientations and nature of boundaries. By following the Mg grains orientation, we noticed that the remaining undeuterated Mg phase with random grain orientation seem to have a slightly coarser lamella eutectic microstructure both before and after deuterium absorption (Fig. 4c and 4f). This observation is supported by the previous studies on cold worked Mg which tends to show strong [0002] grain orientation leading to preferred diffusion pathway for hydrogen [54].

Microstructural changes upon sample activation favor rapid sorption kinetics during the following absorption of deuterium into the Mg particles. In addition to the changes that occur in the core of the particle, the growth of MgD_2 leads to volume expansion and mechanical strains (such modifications that cause decrepitation have been observed as the recovered sample after the experiment is no longer in a compact shape but rather in the form of a loose powder). The splintering of the particles causes the discontinuity of the MgO layer at the particle surface and, hence, the exposure of new surfaces available for the solid-gas reaction.

Once the composite has undergone the activation stage, the desorption process occurs in highly favorable microstructure with deuterium/hydrogen diffusion controlled first by the $Mg_2NiD_4 \rightarrow Mg_2NiD_{0.3-x}$ reaction. This step, which is relatively fast at a pressure of 1.5 bar (the equilibrium pressure being 4 bar at T = 285°C), leads to the rapid desorption of MgH_2 "assisted" by the rapid hydrogen diffusion through the $Mg_2NiD_{0.3-x}$ phase (even faster owing to the high density of Mg-Mg_2Ni boundaries). The experimental conditions chosen (T = 285°C, P = 1.5 bar) does not lead to complete deuterium desorption from the Mg_2Ni deuteride. This corresponds specifically to the existence domain of the solid solution [29], which is a vector of fast deuterium diffusion in the sample.

Further hydrogen/deuterium absorptions in the activated Mg-Mg_2Ni composite start with an increase of the unit cell volume of the $Mg_2NiD_{0.3-x}$ solid solution as an indication of the rapid diffusion of deuterium. As depicted in Fig. 10b, MgD_2 formation begins much faster than during activation with two thirds of Mg transformed in 17 minutes instead of the previous 80 minutes. Kinetic analyses indicate that the diffusion mechanism (CV2/3) is the limiting step since the beginning of the reaction. The rapid nucleation of the MgD_2 phase is associated with the presence of clean surfaces resulting from the delamination of the MgO layer, the presence

of cracks and the large concentration of dislocations induced during the initial deuteration. During the first step (first 17 minutes), Mg_2NiD_4 formation does not occur as a result of thermodynamics: the chemical potential of hydrogen in MgH_2 is more negative than in Mg_2NiH_4. The enthalpy of formation for the binary hydride MgH_2 and Mg_2NiH_4 are $\Delta H_f^0(MgH_2) = -76$ kJ mol^{-1} H_2 [37] and $\Delta H_f^0(Mg_2NiH_4) = -64$ kJ mol^{-1} H_2, respectively [40]. To summarize the second absorption, we observe the very rapid formation of MgD_2 upon D_2 absorption in the second cycle as it is more favorable from a thermodynamic viewpoint. Such rapid deuteration in the second absorption is due to the fact that the first cycle has rendered accessible fresh surfaces and domains of Mg which were initially burried in the sample. However, because D_2 diffusion through MgD_2 is slow, the growth of MgD_2 is hindered as the domain size becomes large (the so-called impingement effect discussed in our paper). As a result, when such slowing down is observed, the second concomitant reaction leading Mg_2NiD_4 becomes predominant. A similar mechanism (featuring the appearance of Mg_2NiD_4 only after around 2/3 of the Mg is converted into MgD_2) has been previously reported for a powdered hypo-eutectic Mg-Ni sample [55] and seems to be favored for samples where fresh surfaces are exposed and facilitate the hydrogen absorption process. This is the case for our sample after activation. By contrast, to our knowledge, the mechanism that we reveal for the first hydrogen absorption, has never been reported. It differs due to the dissimilarity of the initial (massive) state - a critical parameter for solid-gas reactions. The as-forged alloy, roughly crushed into millimeter-sized pieces, is a non-pyrophoric, easy-to-handle bulk material that can be hydrided without prior preparation. We can also note the advantage of the forged sample, which shows a loading time one order of magnitude faster, despite slightly less favorable conditions (PH_2=20b, T= 350°C in ref 55 vs PH_2=20b, T= 285°C in the present work)].

5. Conclusion

In the present work, *in situ* neutron diffraction was used to unravel the deuterium sorption mechanism for a two constituent Mg-Mg_2Ni composite material processed by powder annealing followed by fast forging. The main results can be summarized as follows:

1. The sequence of phase transformation is very different for the first deuteration compared to the subsequent deuterations. Upon the first deuteration (initial activation), the

deuterium uptake proceeds first through the rapid formation of the solid solution $Mg_2NiD_{0.3-x}$. This intermediate phase results from the preferential solubilization of hydrogen into the Mg_2Ni phase (less sensitive to oxidation than pure magnesium). Its rapid formation is a consequence of the fast diffusion of hydrogen within the solid solution $Mg_2NiD_{0.3-x}$ (at least two orders of magnitude higher than in Mg and Mg_2Ni).

2. Upon the first deuteration, MgD_2 nucleates at the Mg-$Mg_2NiD_{0.3}$ interface and its growth rate is controlled by the migration of the Mg/MgD_2 interface. Simultaneously, Mg_2NiD_4 is formed as a result of saturation of the $Mg_2NiD_{0.3-x}$ solid solution. Kinetic modeling indicates that absorption that occurs in the non-activated composite proceeds through a 2D nucleation and growth process. The limiting factor in this case is hydrogen diffusion through the Mg_2NiD_4 plates.

3. Significant microstructural changes, which are beneficial to the fast diffusion of hydrogen, occur upon the activation sequence: twins formation, appearance of cracks and of new oxidation-free surfaces. The twinning system is determined to be {011} <1-11> using the stereographic projections of twinning plane {011} and twinning direction <1-11> and plane trace analysis. Twins accommodate the internal stress and the lattice mismatch between the Mg and MgD_2 phases.

4. Upon the second/third deuteration, the deuterium uptake proceeds from the fast and immediate formation of the MgD_2 phase as a result of the microstructural changes occurring upon activation. The favorable thermodynamical conditions also lead to the growth of the Mg_2NiD_4 phase. Kinetic modeling combined with microstructure observations indicates that absorption (that occurs in the activated composite) proceeds through the nucleation of MgD_2 at the Mg-$Mg_2NiD_{0.3-x}$ interphase boundaries. In this case, the limiting factor is the migration of Mg/MgD_2 interface. In the second stage, the Mg_2NiD_4 formation is kinetically controlled by deuterium diffusion through the growing Mg_2NiD_4 plate. The associated slow diffusion of D_2 in the hydride phases is responsible for the formation of a hydride shell which becomes a diffusion barrier that limits the formation in depth of a fully hydrided composite. While this is out of the scope of the present paper, a possible route to mitigate such diffusion limitations would be to form very finely divided microstructures to boost D_2 diffusion and, hence, accelerate the hydridation kinetics.

5. For the deuterium desorption, as the phase constituents in the deuterated sample are similar, the kinetics behavior is the same for the first and the subsequent desorptions. The release of deuterium always starts from the rapid decomposition of the Mg_2NiD_4 phase into $Mg_2NiD_{0.3-x}$ and deuterium, followed by a rather slow process of the $MgD_2 \rightarrow Mg + D_2$ reaction governed by the rate of deuterium diffusion through the growing Mg phase.

Acknowledgement

The authors acknowledge financial support from the IDEX-CDP Eco-SESA program (Université Grenoble Alpes, France). This work was also supported by the French State through the program "Investment in the future" operated by the National Research Agency (ANR) and referenced by ANR-11-LABX-0008-01 (Labex DAMAS). 2FDN is acknowledged for providing beamtime on CRG-D1b instrument at ILL. Dr. Wen Jing thanks the support from the Natural Science Foundation of China (52201241) and Scientific Research Fund of Liaoning Provincial Education Department (No. JYTMS20230004). We are thankful to V. Nassif, S. Djellit and S. Baudoin for technical support.

References

[1] J. Huot, G. Liang, S. Boily, A. van Neste, R. Schultz, Structural study and hydrogen sorption kinetics of ball-milled magnesium hydride, J. Alloys Compd. 293-295 (1999) 495-500. https://doi.org/10.1016/S0925-8388(99)00474-0

[2] P. Wang, A.M Wang, Y.L Wang, H.F Zhang, Z.Q Hu, Decomposition behavior of MgH2 prepared by reaction ball-milling, Scr. Mater. 43 (2000) 83-87. https://doi.org/10.1016/S1359-6462(00)00370-5

[3] S.D. House, J. J. Vajo, C. Ren, A.A. Rockett, I.M. Robertson, Effect of ball-milling duration and dehydrogenation on the morphology, microstructure and catalyst dispersion in Ni-catalyzed MgH2 hydrogen storage materials, Acta Mater. 86 (2015) 55-68. https://doi.org/10.1016/j.actamat.2014.11.047

[4] S. Rousselot, D. Guay, L. Roué, Comparative study on the structure and electrochemical hydriding properties of MgTi, $Mg_{0.5}Ni_{0.5}Ti$ and $MgTi_{0.5}Ni_{0.5}$ alloys prepared by high energy ball milling, J. Power Sources 196 (2011) 1561-1568. https://doi.org/10.1016/j.jpowsour.2010.09.008

[5] S. Kalinichenka, L. Röntzschb, B. Kieback, Structural and hydrogen storage properties of melt-spun Mg-Ni-Y alloys, Int. J. Hydrogen Energy 34 (2009) 7749-7755. https://doi.org/10.1016/j.ijhydene.2009.07.053

[6] X.J. Hou, R. Hu, T.B. Zhang, H.C. Kou, J.S. Li, Hydrogenation thermodynamics of melt-spun magnesium rich Mg-Ni nanocrystalline alloys with the addition of multiwalled carbon nanotubes and TiF_3, J. Power Sources 306 (2016) 437-447. https://doi.org/10.1016/j.jpowsour.2015.12.050

[7] T. Hongo, K. Edalati, M. Arita, J. Matsuda, E. Akiba, Z. Horita, Significance of grain boundaries and stacking faults on hydrogen storage properties of Mg2Ni intermetallics processed by high-pressure torsion, Acta Mater. 92 (2015) 46-54. https://doi.org/10.1016/j.actamat.2015.03.036

[8] J. Huot, S. Amira, J. Lang, N. Skryabia, D. Fruchart, Improvement of hydrogen properties of magnesium alloys by cold rolling and forging, Mater. Sci. Eng. 63 (2014) 012-114. https://doi.org/10.1088/1757-899X/63/1/012114

[9] A. Revesz, M. Gajdics, E. Schafler, M. Calizzi, L. Pasquini, Dehydrogenation hydrogenation characteristics of nanocrystalline Mg_2Ni powders compacted by high-pressure torsion, J. Alloys Compd. 702 (2017) 84-91. https://doi.org/10.1016/j.jallcom.2017.01.261

[10] D. Chen, Y.M. Wang, L. Chen, S. Liu, C.X. Ma, L.B. Wang, Alloying effects of transition metals on chemical bonding in magnesium hydride MgH2, Acta Mater. 52 (2004) 521-528. https://doi.org/10.1016/j.actamat.2003.09.037

[11] J. Wen, P. de Rango, N. Allain, L. Laversenne, T. Grosdidier, Improving hydrogen storage performance of Mg-based alloy through microstructure optimization, J. Power Sources 480 (2020) 228823. https://doi.org/10.1016/j.jpowsour.2020.228823

[12] J. Wen, L. Laversenne, M. Novelli, T. Grosdidier, P. deRango, In situ analysis of phase constituents evolution upon hydrogen cycling of cold-forged Mg-Ni powders, J. Alloys Compd. 947 (2023) 169543. https://doi.org/10.1016/j.jallcom.2023.169543.

[13] S. Hayashi, K. Hayamizu, O. Yamamoto, 1H NMR study of the α phase of Mg2NiHx system, J. Phys. Chem. Solids 45 (1984) 555-562. https://doi.org/10.1016/0022-3697(84)90090-8.

[14] A. Zaluska, L. Zaluski, J.O. Ström-Olsen, Synergy of hydrogen sorption in ball-milled hydrides of Mg and Mg2Ni, J. Alloys Compd. 289 (1999) 197-206. https://doi.org/10.1016/S0166-0462(99)00013-7

[15] R.V. Denys, A.B. Riabov, J.P. Maehlen, M.V. Lototsky, J.K. Solberg, V.A. Yartys, In situ synchrotron X-ray diffraction studies of hydrogen desorption and absorption properties of Mg and Mg-Mm-Ni after reactive ball milling in hydrogen, Acta Mater. 57 (2009) 3989-4000. https://doi.org/10.1016/j.actamat.2009.05.004

[16] X.Q. Tran, S.D. McDonald , Q.F. Gu, et al. In-situ investigation of the hydrogen release mechanism in bulk Mg_2NiH_4, J. Power Sources 341 (2017) 130-138. https://doi.org/10.1016/j.jpowsour.2016.11.105.

[17] S. Orimo, H. Fujii, Materials science of Mg-Ni-based new hydrides, Appl. Phys. A 72, (2001) 167-186. https://doi.org/10.1007/s003390100771

[18] S. Isobe, A. Ono, H. Yao, Y. Wang, N. Hashimoto, S. Ohnuki, Study on reaction mechanism of dehydrogenation of magnesium hydride by in situ transmission electron microscopy, Appl. Phys. Lett. 96 (2010) 223109. https://doi.org/10.1063/1.3442910

[19] M. Danaie, D. Mitlin, TEM analysis of the microstructure in TiF_3-catalyzed and pure MgH_2 during the hydrogen storage cycling, Acta Mater. 60 (2012) 6441-6456. https://doi.org/10.1016/j.actamat.2012.07.036

[20] C. Zhu, N. Sakaguchi, S. Hosokai, S. Watanabe, T. Akiyama, In situ transmission electron microscopy observation of the decomposition of MgH_2 nanofiber, Int. J. Hydrogen Energy 36 (2011) 3600-3605. https://doi.org/10.1016/j.ijhydene.2010.12.017

[21] X. Sauvage, S. Moldovan, F Cuvilly, M Bahri, T Grosdidier, In-situ transmission electron microscopy investigation of the influence of hydrogen on the oxidation mechanisms of fine grained magnesium, Mater. Chem. Phys. 248 (2020) 122928. https://doi.org/10.1016/j.matchemphys.2020.122928

[22] M. Tanaka, S. Sadamatsu, G.S. Liu, H. Nakamura, K. Higashida, I.M. Robertson, Sequential multiplication of dislocation sources along a crack front revealed by high-voltage electron microscopy and tomography, J. Mater. Res. 26 (2011) 508-513. https://doi.org/10.1557/jmr.2010.99

[23] N. Bourgeois, J.C. Crivello, P. Cenedese, V.P. Boncour, J.M. Joubert, Vibration analysis of hydrogen, deuterium and tritium in metals: consequences on the isotope effect, J. Phys.: Condens. Matter 30 (2018) https://doi.org/10.1088/1361-648X/aad259

[24] J. Rodriguez-Carvajal, Recent developments of the program FULLPROF, Commission Powder Diffraction Newslett. 26 (2001) 12-19.

[25] B. Beausir, J.J. Fundenberger, Analysis Tools for Electron and X-Ray Diffraction, Université de Lorraine - Metz, 2017. ATEX - software, www.atex-software.eu.

[26] F. Zimmermann, M. Humbert, Determination of the habit plane characteristics in the β–α' phase transformation induced by stress in Ti-5Al-2Sn-4Zr-Mo-2Cr-1Fe, Acta Mater. 50 (2002) 1735-1740. https://doi.org/10.1016/S1359-6454(02)00022-8

[27] J. Jiang, A. Godfrey, W. Liu, Q. Liu, Identification and analysis of twinning variants during compression of a Mg-Al-Zn alloy, Scr. Mater. 58 (2008) 122-125. https://doi.org/10.1016/j.scriptamat.2007.09.047

[28] M. Liu, Y. Zhang, X. Wang, B. Beausir, X. Zhao, L. Zuo, C. Esling, Crystal defect associated selection of phase transformation orientation relationships (ORs), Acta Mater. 152 (2018) 315-326. https://doi.org/10.1016/j.actamat.2018.04.031

[29] J. Schefer, P. Fischer, W. Hälg, F. Stucki, L. Schlapbach, J.J. Didisheim, K. Yvon, A.F. Andresen, New structure results for hydrides and deuterides of the hydrogen storage material Mg2Ni, J. Less-Common Met. 74 (1980) 65-73. https://doi.org/10.1016/0022-5088(80)90074-0

[30] B. Darriet, J.L. Soubeyroux, M. Pezat, D. Fruchart, Structural and hydrogen diffusion study in the Mg2Ni-H2 system, J. Less-Common Met. 103 (1984) 153-162. https://doi.org/10.1016/0022-5088(84)90374-6

[31] I. Saita, L.Q. Li, K. Saito, T. Akiyama, Hydriding combustion synthesis of Mg2NiH4, J. Alloys Compd. 356-357 (2003) 490-493. https://doi.org/10.1016/S0925-8388(03)00230-5

[32] Y.N. Wang, J.C. Huang, Texture analysis in hexagonal materials, Mater. Chem. Phys. 81 (2003) 11-26. https://doi.org/10.1016/S0254-0584(03)00168-8

[33] S.K. Sahoo, S. Biswas, L.S. Toth, P.C. Gautam, B. Beausir, Strain hardening, twinning and texture evolution in magnesium alloy using the all twin variant polycrystal modelling approach, Int. J. Plast. 128 (2020) 102660. https://doi.org/10.1016/j.ijplas.2020.102660

[34] M. Danaie, S.X. Tao, P. Kalisvaart, D. Mitlin, Analysis of deformation twins and the partially dehydrogenated microstructure in nanocrystalline magnesium hydride (MgH_2) powder, Acta Mater. 58 (2010) 3162-3172. https://doi.org/10.1016/j.actamat.2010.01.055

[35] S.X. Tao, W.P. Kalisvaart, M. Danaie, D. Mitlin, P.H.L. Notten, R.A. van Santen, A.P.J. Jansen, First principle study of hydrogen diffusion in equilibrium rutile, rutile with deformation twins and fluorite polymorph of Mg hydride, Int. J. Hydrogen Energy 36 (2011) 11802-11809. https://doi.org/10.1016/j.ijhydene.2011.06.075

[36] H. Emami, K. Edalati, J. Matsuda, E. Akiba, Z.J. Horita, Hydrogen storage performance of TiFe after processing by ball milling, Acta Mater. 88 (2015) 190-195. https://doi.org/10.1016/j.actamat.2014.12.052

[37] J.A. Kammerer, X.Y. Duan, F. Neubrech, R. R Schröder, N. Liu, M. Pfannmöller, Stabilizing γ-MgH_2 at Nanotwins in Mechanically Constrained Nanoparticles, Adv. Mater 33 (2021) 2008259. https://doi.org/10.1002/adma.202008259

[38] M. Avrami, Kinetics of phase change. II transformation-time relations for random distribution of nuclei, J. Chem. Phys. 8 (1940) 212-224. https://doi.org/10.1063/1.1750631

[39] M. Avrami, Granulation, Phase Change, and Microstructure Kinetics of Phase Change, J. Chem. Phys. 9 (1941) 177-184. https://doi.org/10.1063/1.1750872

[40] A. Borgschulte, R. Gremaud, R. Griessen, Interplay of diffusion and dissociation mechanisms during hydrogen absorption in metals, Phys. Rev. B 78 (2008) 094106. https://doi.org/10.1103/PhysRevB.78.094106

[41] N. Koga, J.M. Criado, Kinetic analyses of solid-state reactions with a particle-size distribution, J. Am Ceram Soc. 81 (1998) 2901-2909. https://doi.org/10.1111/j.1151-2916.1998.tb02712.x

[42] J.F. Fernandez, C.R. Sanchez, Rate determining step in the absorption and desorption of hydrogen by magnesium, J. Alloys. Compd. 340 (2002) 189-198. https://doi.org/10.1016/S0925-8388(02)00120-2

[43] W. Jander, Reaktionen im festen Zustande bei höheren Temperaturen. Reaktions geschwindigkeiten endotherm verlaufender Umsetzungen, Z. Anorg. Allg. Chem. 163 (1927) 1-30 (in German).

[44] J.W. Christian, Formal Theory of Transformation Kinetics, The Theory of Transformations in Metals and Alloys, Pergamon: Oxford; 2002. pp. 529-552. https://doi.org/10.1016/B978-008044019-4/50016-7

[45] J. Cermak, L. Kral, B. David, Hydrogen diffusion in Mg2NiH4 intermetallic compound, Intermetallics 16 (2008) 508-517. https://doi.org/10.1016/j.intermet.2007.12.010

[46] J. Čermák, L. Král, Hydrogen diffusion in Mg-H and Mg-Ni-H alloys, Acta Mater. 56 (2008) 2677-2686. https://doi.org/10.1016/j.actamat.2008.02.003

[47] H.Y. Tien, M. Tanniru, C.Y. Wu, F. Ebrahimi, Effect of hydride nucleation rate on the hydrogen capacity of Mg, Int. J. Hydrogen Energy 34 (2009) 6343-6349. https://doi.org/10.1016/j.ijhydene.2009.06.008

[48] M. Dornheim, S. Doppiu, G. Barkhordarian, U. Boesenberg, T. Klassen, O. Gutfleisch and R. Bormann, Hydrogen storage in magnesium-based hydrides and hydride composites, Scr. Mater. 56 (2007) 841-846. https://doi.org/10.1016/j.scriptamat.2007.01.003

[49] L. Schlapbach, D. Shaltiel, P. Oelhafen, Catalytic effect in the hydrogenation of Mg and Mg compounds: Surface analysis of Mg-Mg2Ni and Mg2Ni, Mater. Res. Bull. 14 (1979) 1235-1246. https://doi.org/10.1016/0025-5408(79)90220-4

[50] J. Karst, F. Sterl, H. Linnenbank, T. Weiss, M. Hentschel, H. Giessen, Watching in situ the hydrogen diffusion dynamics in magnesium on the nanoscale, Sci. Adv. 6 (2020) eaaz0566. https://doi.org/10.1126/sciadv.aaz0566

[51] T. Schober, The magnesium-hydrogen system: Transmission electron microscopy, Metall. Trans. A. 12 (1981) 951-957. https://doi.org/10.1007/BF02643475

[52] G.C. Weatherly, The precipitation of γ-hydride plates in zirconium, Acta Metall. 29 (1981) 501-512. https://doi.org/10.1016/0001-6160(81)90074-2

[53] O.T. Woo, G.C. Weatherly, C.E. Coleman, R.W. Gilbert, The precipitation of γ-deuterides (hydrides) in titanium, Acta Metall. 33 (1985) 1897-1906. https://doi.org/10.1016/0001-6160(85)90011-2

[54] X.F. Tan, M.J. Kim, K. Yasuda, K. Nogita, Strategies to enhance hydrogen storage performances in bulk Mg-based hydrides, J. Mater. Sci. Technol. 153 (2023) 139-158. https://doi.org/10.1016/j.jmst.2022.12.054

[55] X. Q. Tran, S. D. McDonald, Q. Gu, X. F. Tan, K. Nogita, Effect of trace Na additions on the hydriding kinetics of hypo-eutectic Mg-Ni alloys, Int. J. Hydrogen Energy 42 (2017) 6851-6861. https://doi.org/10.1016/j.ijhydene.2016.12.007